PROCEEDINGS OF SPIE

SPIEDigitalLibrary.org/conference-proceedings-of-spie

PLATO EM first cryogenic vacuum test campaign PSF results

Francesco Borsa, Andrea Cottinelli, Nicolas Gorius, Claudio Arena, Bart Vandenbussche, et al.

Francesco Borsa, Andrea Cottinelli, Nicolas Gorius, Claudio Arena, Bart Vandenbussche, Sara Regibo, Rik Huygen, Pierre Royer, Martin Pertenais, Cesar Martin, Thierry Appourchaux, Jose Lorenzo Alvarez, Tim A. van Kempen, Wouter Laauwen, Isabella Pagano, Roberto Ragazzoni, "PLATO EM first cryogenic vacuum test campaign PSF results," Proc. SPIE 12180, Space Telescopes and Instrumentation 2022: Optical, Infrared, and Millimeter Wave, 121801D (27 August 2022); doi: 10.1117/12.2630118

SPIE.

Event: SPIE Astronomical Telescopes + Instrumentation, 2022, Montréal, Québec, Canada

PLATO EM first cryogenic vacuum test campaign PSF results

Francesco Borsa[a], Andrea Cottinelli[b], Nicolas Gorius[c], Claudio Arena[c], Bart Vandenbussche[d], Sara Regibo[d], Rik Huygen[d], Pierre Royer[d], Martin Pertenais[e], Cesar Martin[e], Thierry Appourchaux[f], Jose Lorenzo Alvarez[g], Tim A. van Kempen[h], Wouter Laauwen[i], Isabella Pagano[c], and Roberto Ragazzoni[b,l]

[a]INAF – Osservatorio Astronomico di Brera, Via E. Bianchi 46, 23807 Merate (LC), Italy
[b]INAF – Osservatorio Astronomico di Padova, Vicolo dell'Osservatorio 5, 35122, Padova, Italy
[c]INAF – Osservatorio Astrofisico di Catania, Via S.Sofia 78, 95123, Catania, Italy
[d]Institute of Astronomy, KU Leuven, Celestijnenlaan 200D bus 2401, 3001 Leuven, Belgium
[e]German Aerospace Center (DLR), Institute of Optical Sensor Systems, Rutherfordstr. 2, 12489 Berlin, Germany
[f]IAS, UMR8617, Université Paris-Saclay, Bâtiment 121, 91405 Orsay, France
[g]European Space Agency, The Netherlands
[h]SRON Netherlands Institute for Space Research, Niels Bohrweg 4, 2333 CA, Leiden, The Netherlands
[i]SRON Netherlands Institute for Space Research, Landleven 12, Groningen, The Netherlands
[l]Università degli Studi di Padova, via VIII Febbraio, 2, Padova, Italy

ABSTRACT

PLATO (PLAnetary Transits and Oscillations of stars) is a European Space Agency medium class mission, whose launch is foreseen for 2026. Its primary goal is to discover and characterise terrestrial exoplanets orbiting the habitable zone of their host stars. This goal will be reached with a set of 26 wide field-of-view cameras mounted on a common optical bench. Here we show some results of the first cryogenic vacuum test campaign made on the Engineering Model (EM) of one PLATO camera, performed at the Netherlands Institute for Space Research (SRON). In particular we present the search for the best focus temperature, which was done first by using a Hartmann mask, and then by maximizing the ensquared energy fractions of the point spread functions (PSFs) on the entire field of view taken at different temperature plateaus. Furthermore we present the PSF properties of the EM at the nominal focus temperature over all the field of view, focusing on the ensquared energy fractions. The Engineering Model camera was successfully integrated and validated under cryo-vacuum tests, allowing the mission to pass ESA's Critical Milestone, and confirming the mission is on track for launch in 2026.

Keywords: PLATO, PSF, Best focus search, Hartmann mask, Ensquared energy fractions

1. INTRODUCTION

PLATO (PLAnetary Transits and Oscillations of stars)[1] is the Cosmic Vision Programme M3 mission selected by ESA for launch in 2026. Its goal is to discover and characterize exoplanets through high-precision, long-term photometric monitoring of a large number of bright stars. The PLATO payload includes 24 'normal' cameras, with CCD-based focal planes, operating in white light (500-1000nm wavelength range), plus two additional *coloured* 'fast' cameras (blue 500-675nm, red 675-1000nm).[2] Each camera is based on the same fully dioptric design, a refractive system made of six lenses plus one window placed at the entrance of the telescope, with a 120 mm entrance pupil and an effective field of view of $\sim$1100 deg^2 ($\sim$ 33 degrees x 33 degrees).[3,4] The focal plane array is made of 4 CCDs each with 4510x4510 pixels of 18 μm size, working in full frame mode for the 'normal'

Further author information: Send correspondence to F. Borsa
E-mail: francesco.borsa@inaf.it

Space Telescopes and Instrumentation 2022: Optical, Infrared, and Millimeter Wave, edited by Laura E. Coyle, Shuji Matsuura, Marshall D. Perrin, Proc. of SPIE Vol. 12180, 121801D · © 2022 SPIE · 0277-786X · doi: 10.1117/12.2630118

cameras and in frame transfer mode for the 'fast' cameras. The huge field of view of PLATO, with a roundish square footprint of about 49 x 49 degrees overall, will simultaneously image about 5% of the whole sky.

In the framework of the verification of the performances, testing and calibrations of the PLATO camera at operational conditions, a first campaign of cryogenic vacuum tests on the Engineering Model (EM) Camera has been done at the Netherlands Institute for Space Research (SRON). A fixed collimator illuminates the entrance pupil of the EM camera using a source which is representing a PLATO reference star. The camera is fixed in a gimbal allowing to rotate it and access with the source the complete scientific field of view. A detailed description of the test facility and setup can be found in Refs.,[5,6] together with a test plan.

In this manuscript we present the best focus temperature (BFT) search and the performances of the PSF on the whole field of view (FoV) at the best focus temperature.

2. SEARCHING FOR THE BEST FOCUS TEMPERATURE

The BFT has been searched using two complementary methods. At first, during the cooldown phase, we used a Hartmann mask (Sect. 2.1). Then we verified the BFT, expected close to -80°C, by optimising the ensquared energies fractions (EEFs) of the 2x2 versus 10x10 pixels on the whole FoV taken at five different temperatures plateaus of -70, -75, -80, -85, -90 °C (Sect. 2.2, see Ref.[7]). A detailed description of the cryo-vacuum tests performed at SRON is reported in Ref.[5] .

2.1 Hartmann mask method

In the Hartmann mask method, a grid of pinholes is placed in the pupil plane. In our case, the mask was made of 9 pinholes on a circle. The goal of the test is to estimate the focal plane position (in our case, the best focusing temperature) by interpolating both the size of the pattern and the virtual light rays passing through the pinholes at different temperatures. The pattern projected on the image plane shrinks due to thermal focusing as the temperature decreases. Hartmann data were taken during the cool-down phase to verify the correct functioning of thermal focusing and to make a first rough prediction of the best focus temperature. Data were acquired between +17.8°C and -18°C in 20 positions in a 8.3 deg ring around the optical axis (Fig. 1, left panel).

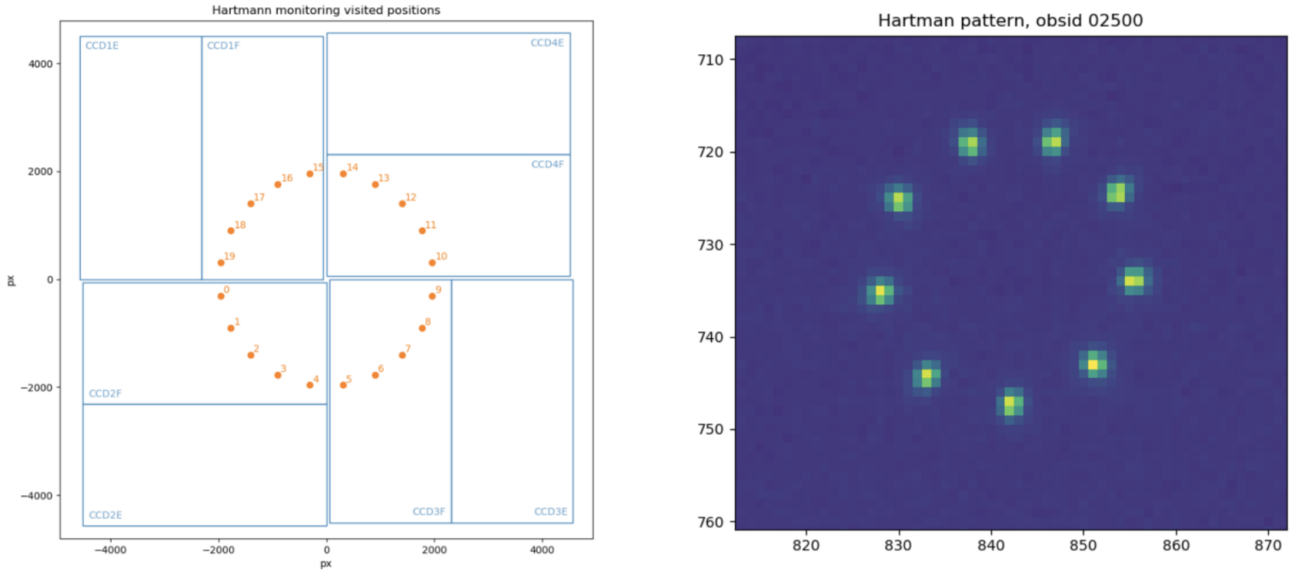

Figure 1: (Left panel) Positions on the FoV where the Hartmann mask data were acquired. (Right panel) Example of an Hartmann mask image, with the light passing through the 9 pinholes.

The mask used comprises 9 pinholes arranged circularly and has been positioned on the pupil. It has to be specified that this is not the common use of the Hartmann mask test. Here, we made the strong assumption

that there is linearity between cooling rate and thermal focusing, so the rays passing through the spots of the Hartmann pattern can be fitted as straight lines. The different analyses performed during the tests show that this is an approximation.

We analysed our dataset following the method detailed in Ref.[8] . Briefly, each image was first corrected for background and we averaged the two consecutive images taken for each position. A Gaussian filter was then applied and a search algorithm highlighted the 9 peaks of the Hartmann mask. A 7x7 pixel window was then cut around each local maximum and we then refined the correct position of the centroid, that was defined as the mean position in x and y weighted in flux. The 9 centroids thus obtained were stored separately and then analyzed for comparison with the other images.

2.1.1 Rays extrapolation

Following what has been done to characterize the best focal plane at Telescope Optical Unit (TOU) level[8] , the rays extrapolation method consists of numbering the holes of the mask on the images to reconstruct the rays that pass through them, as shown in Fig. 2. Then, the rays are extrapolated to find the temperature that minimizes their distance or RMS.

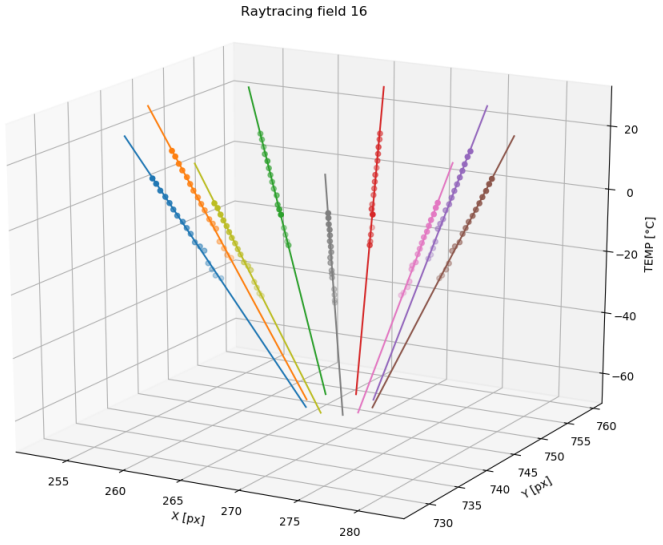

Figure 2: Example of rays extrapolation for a single field.

The average above the field of view is used as a raw prediction of BFT. Results are shown in Fig. 3. BFT predicted by rays extrapolation is -80.3 ± 1.3°C. The error-bar is calculated as the dispersion of the values of the different fields. We suppose there are other contributions to the error, such as the non-linearity of thermal focusing. During the data analysis, that was done in real time while the cooldown was ongoing, the data in fact showed a non-linear relationship between temperature and estimation of the best focus temperature. In particular, for hotter temperatures the BFT was predicted to be colder, while for the colder ones the BFT was predicted hotter. Furthermore, we are using the Hartmann mask only on a ring on the focal plane (Fig. 1, left panel) instead of on the entire FoV, which was instead used to estimate the BFT when using the PSF method with the five temperatures plateaus (Sect. 2.2) and is thus more adapt to compute the BFT for the whole FoV. After looking at the non linearity, we consider then a $\sim \pm 5$°C error-bar more plausible on our Hartmann mask BFT estimation. We however were able to see that with a first estimation done during the first cooldown the BFT was in line with what expected from design.

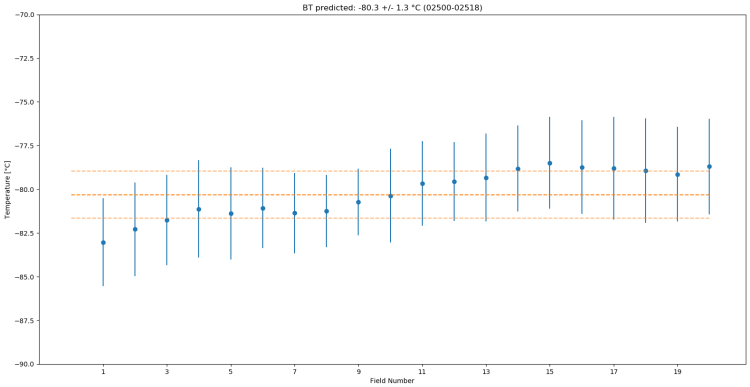

Figure 3: Hartmann mask BFT prediction via rays extrapolation for each of the 20 field positions analyzed. Horizontal orange lines show the average value and its 1σ dispersion.

2.2 PSF method: maximizing ensquared energy functions

As our main and default approach, we tested the BFT by maximizing the ensquared energy fractions of 2x2 pixels over all the energy of the PSF.

By instrumental design, the BFT is expected to be close to -80°C.[3] We tested the EM at five different temperature plateaus, from -70°C to -90°C in step of 5°C,[7] and then analyzed how the performances of the PSFs (in particular of the ensquared energy fractions 2x2/10x10 pixels) changed with varying the temperature. Particular attention was taken in order to reach the temperature stability of the system after each temperature change.

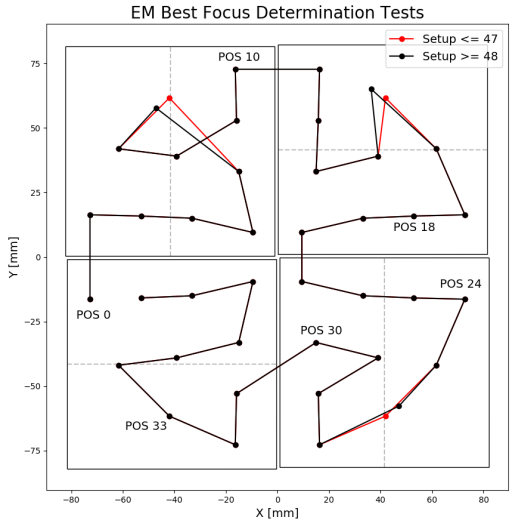

Figure 4: The 40 positions on the FoV where the EEFs of the PSFs have been measured at the 5 temperature plateaus, for the best focus temperature search. Three positions were corrected during the analysis as their PSFs were falling between the edges of CCD sides.

We sampled the FoV in 40 equi-spaced positions, as shown in Fig. 4.

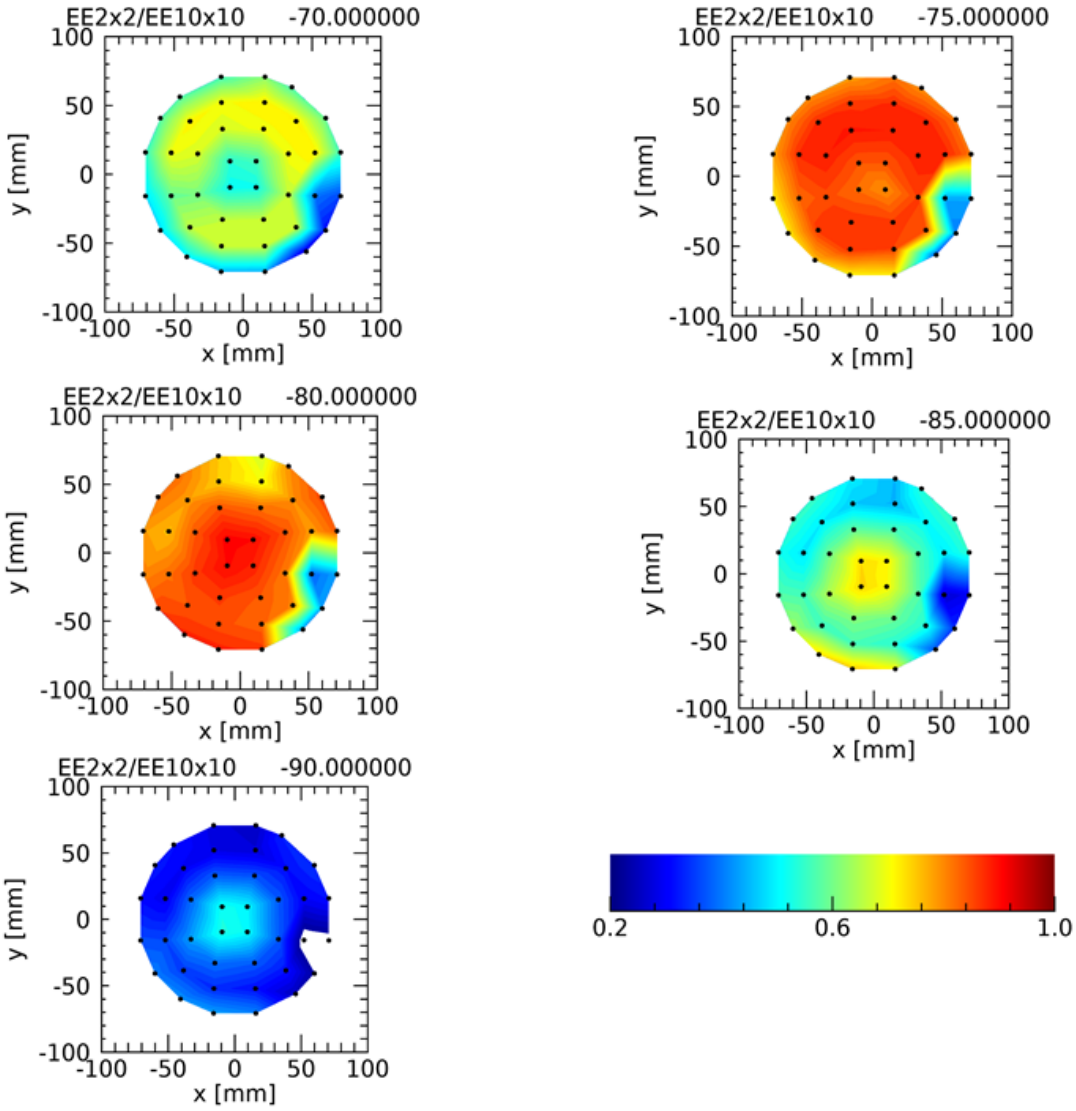

Figure 5: For the five temperatures plateaus, field of view map plotted in focal plane coordinates, with each black point corresponding to a measurement point. Color code corresponds to the Ensquared Energy Fraction 2x2 pixels to 10x10 pixels. 2D parabolic interpolation was used to compute the EEF values in-between measurement points.

For each of the 40 positions we took 25 dithering sub-pixel positions, we estimate their EEF2x2 and select the maximum one, and then take the average of the EEF2x2 of the 40 positions. The sub-pixel dithering was introduced to minimize the impact of the PSF centroid position on the pixel grid. We describe the method of the EEF extraction in Sect. 2.2.1.

2.2.1 Ensquared energy extraction

The general concept is to extract for each field position the maximum ensquared energies (EE) 1x1, 2x2, 5x5, 7x7, 10x10 pixels from the 25 dithered positions, and then verify if the respective requirements for the EEFs at the BFT are respected on the whole FoV. The first step of the analysis consists in subtracting the background. Here we have two possible methods: the subtraction of the dark frames taken just before the images, or the

subtraction of a median of the same image taken in a square region much larger than the PSF, i.e., a square region of 60x60 pixels centered on the PSF. The two methods revealed themselves to be fully consistent with each other through the analysis. In this manuscript we show the results using the subtraction of the dark frames.

The EEF in NxN pixels is defined as the fraction of energy of the complete PSF that is included inside a square of NxN pixels, with respect to the total energy of the PSF. For definition of requirements, the total energy of the PSF is the energy taken inside a square of 7x7 pixels. In order to compute it, we need to find the EE of the NxN pixel square that contains the highest value of energy and compare it to the EE of the complete PSF (7x7 pixels). For safety, as far as we saw that this nominal 7x7 had the risk of cutting the edges of the PSF in some cases during the tests when going particularly out-of-focus (and indeed we go out-of-focus for the best focus search), for the BFT determination we used as reference the ensquared energy 10x10 pixels. So when speaking of EEFs, in this Section we refer to the normalization of the ensquared energy with respect to the ensquared energy extracted from a square of 10x10 pixels.

For each of the 40 field positions, we have 40x25x4 images, where 25 is the number of dithered positions and 4 is the number of images taken for each dithering. For each dithering we first take the median of the 4 images, excluding the first one (which is always saturated). The median is preferred to the average in order to avoid cosmic rays to introduce spurious noise in the data. Then we calculate the EE 1x1, 2x2, 5x5, 7x7, 10x10 for each dithering, by taking the maximum value of energy among each possible combination of squares of NxN pixels. Then the EEF NxN was calculated as the ratio between EE NxN and EE 10x10 for each dithering position. The EEF NxN for each field is taken as the maximum EEF of the 25 dithered sub-pixel positions.

Error-bars estimation on the extracted EEFs are worth a discussion. The error-bars on the values here presented are first extracted for each pixel by assuming Poissonian noise, i.e., the error-bar for each pixel is the square root of the number of counts of the pixel. Poissonian noise is assumed on the median of the 3 images taken for each dithering (3 and not 4, as the first one is always saturated). If we would have taken the mean instead of the median, then the error should have been reduced by a factor of 1.732 ($\sqrt{(3)}$). Since we took the median in order to exclude the possible contamination caused by cosmic rays, we do not apply this division, as this would not be statistically correct. An error on the median has a formula only if the sample is large (error of the mean * 1.2533), which is not the case with just three images. We thus keep the error taken as the Poissonian noise on the median, knowing that we are somehow slightly overestimating error-bars. Error-bars are then propagated by using standard formulae of error propagation when calculating error-bars of the ensquared energies and of ensquared energy fractions.

We note that the analyses here produced were done using the internal sync readout scheme (partial readout), which enables shorter integration time, faster frame rate and therefore shorter test duration by one order of magnitude, strongly limiting also the hard-drive space and memory required to download and analyse the images. While the full analysis on the external sync readout scheme is still ongoing, preliminary results show a full agreement between the two.

2.2.2 Best focus temperature estimation

At this point we have 5 temperatures with EEF2x2 calculated on the whole FoV (Fig. 5), with an average EEF2x2 for each temperature, and we have to decide how to estimate the BFT. By looking at Fig. 5, it was already evident that the BFT was between -75°C and -80°C. We also already note the presence of few outlier points, all on one side of CCD3 (bottom right of the FoV maps). This problem was already identified ahead of this test and is present because the CCDs on the EM Camera are not flight-grade, and in particular one side of CCD3 suffered from strong pixel crosstalk. These points were rejected during the analysis, without however significantly changing final results.

In Fig. 5 we also observe a clear FoV dependance of the BFT: the center of the field of view seems to reach its best focus at a lower temperature (close to -80°C), while its the opposite for the outer FoV positions (closer to -75°C). Our goal is to maximize the average EEF over all the FoV.

For the best focus determination, several different fitting techniques were proposed, tested and compared with each other. Our baseline, which is also the main approach we present in this work, was to fit a 2nd degree polynomial fit on the average EEFs of the 5 temperature plateaus (Fig. 6).

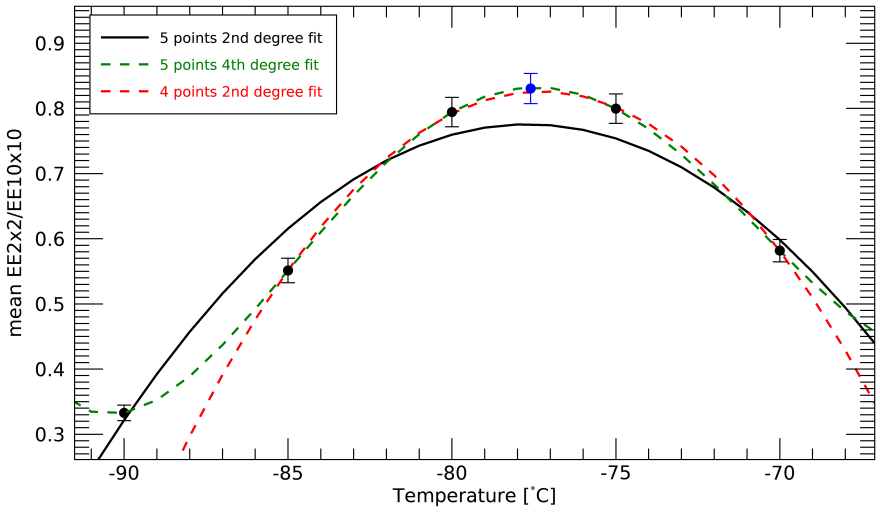

Figure 6: The black points represent the average EEF2x2 taken at the temperature plateaus from -70°C to -90°C. Different lines show the different fits performed to find the best focus temperature. The blue point represents the average EEF2x2 measured at the BFT.

While analyzing the data, we realized that the 2nd degree polynomial fit was clearly more adapt to the data when using only the four temperatures closer to the BFT (Fig. 6). This was also lately verified when taking the measurements at the estimated BFT. Fitting the 2nd degree polynomial only to the data points of the plateaus taken at -85°C, -80°C, -75°C and -70°C clearly provides a better chi-square. This is understandable when thinking that the parabolic behaviour is valid only close to the BFT. But taking only 4 temperature points has a strong drawback, which is the dependance on the choice of which measurement point to take into account and which to ignore, without having strong physical and objective reasons for discarding a point.

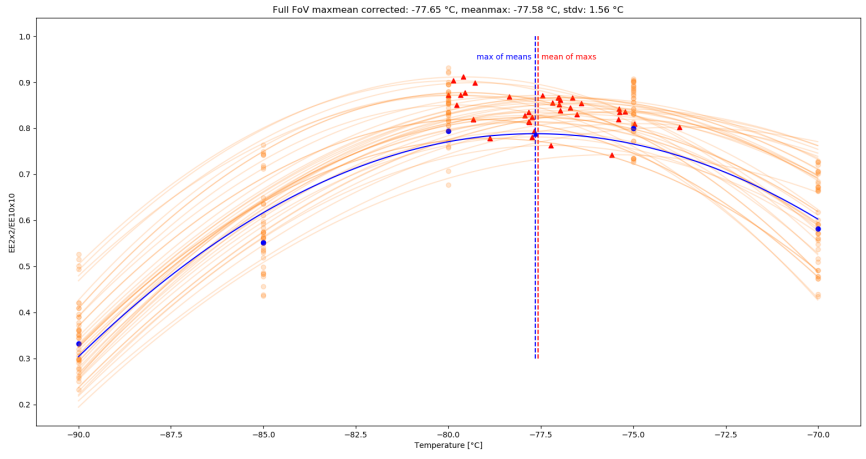

Figure 7: The 5 blue dots correspond to the average EEF for each 5 temperatures, while the red points to the BFT calculated for each position.

A similar approach is, instead of computing the average EEF for each temperature and then fitting a polynomial to these points, to first fit a function (which is always a 2nd degree polynomial) on the 5 temperatures points for each of the 40 FoV positions independently and then take the average of these 40 local best focus temperatures (Fig. 7).

We tried also different approaches, for example the use of a higher degree polynomial (see Fig. 6). Probably the best way to calculate the BFT would be to fit a custom simulated function calculated with a theoretical as-built Zemax model, but in any case this would never perfectly match the exact function of the real EM.

In the end, when comparing the results from the different methods and the analyses from different analysts that were using different codes, we found a strong agreement between all the methods tested (Fig. 6), with differences among the estimated BFT of $\sim$0.1°C, which is well within the expected error-bar. We find a best focus temperature of -77.6°C. This temperature is perfectly matching the requirements. The agreement of the measurements done with the Hartmann mask method and the different PSF methods makes us further confident on the results.

3. PSF AT BEST FOCUS TEMPERATURE

The main objective of this test was to verify that all the specifications and requirements at the best focus temperature were valid for the measurements made at the derived best focus temperature of -77.6°C (Sect. 2). This allowed us to validate the BFT selection method and to characterize the performances at this temperature.

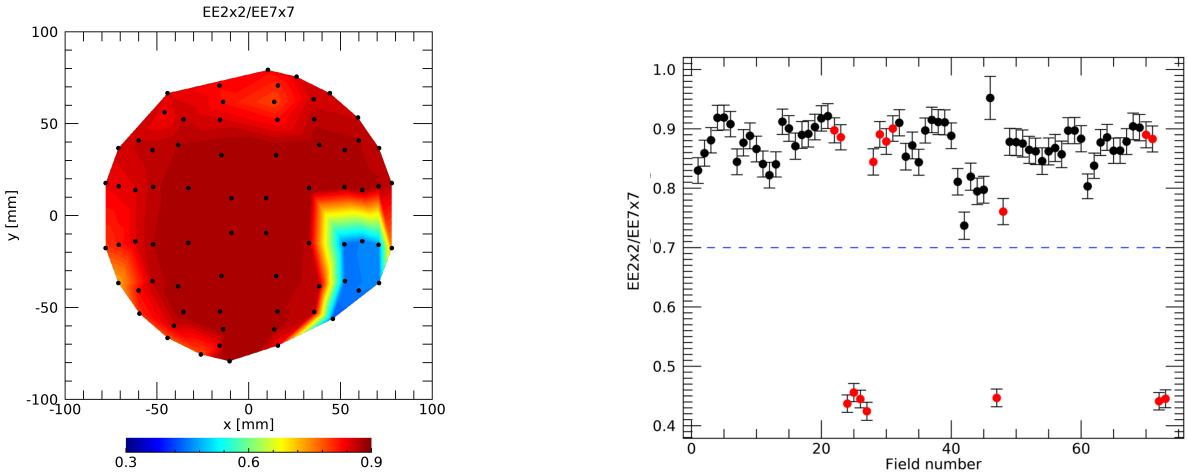

(a) (b)

Figure 8: (a) Contour map for the EEF2x2 calculated at the best focus temperature through the FoV. (b) Values of EEF2x2 calculated at the best focus temperature for the various positions tested through the FoV. Red dots mark the positions taken on CCD3. Horizontal blue dashed line shows the requirement.

The methods used for the data analysis of this test follow the principles and ideas of those used for the analysis of BFT (Sect. 2). Here below we resume the main steps. Particular attention was paid to the choice of the method of integration. For each of the 40 field positions, there are 25 dithering sub-pixel positions. For each dithering position, there are 4 images and 2 dark frames. The general concept is to extract for each field position the maximum ensquared energies (EE) 1x1, 2x2, 5x5, 7x7, 10x10 pixels from the 25 dithered positions, and then verify if the requirements for the EEFs at the BFT are respected on the whole FoV. We first subtracted the background and averaged the 4 images (excluding the first one, saturated). Then we extracted the EEs, calculated the EEFs normalizing them to EE7x7 as per requirement and maximized them over the 25 dithered positions. We stress that, differently to the previous one, in this Section we refer to the EEF weighted over the 7x7 pixel square, as per requirement, as we are doing in-focus measurements.

The results of the EEF calculations at the BFT were found fully matching the requirements. First of all, as shown in Fig. 6, we can see that the EEF2x2 are perfectly in line with those predicted from the analysis of the

5 temperature plateaus during the best focus temperature search (Sect.2). Here the error-bars are calculated as the standard deviation of the 40 measurements for each temperature plateau.

As it can be seen from Fig. 8, the EEF2x2 results are perfectly matching the requirements.

3.1 Comparison after thermal cycling

After the BFT determination and the PSF measurements at the BFT (Sect. 3), the EM model has been stressed with thermal cycling,[5,6] in order to test the stability of the whole camera to thermal stresses. In particular, the temperature was changed between -100°C and -60°C three times.

We analysed the stability of the EEFs of the PSFs after the thermal cycling by comparing measurements done at the BFT before and after thermal cycling. Both the commands used to take the data and the data analysis were the same. As shown in Fig. 9, the stability of the system is well demonstrated, bringing to average differences in the EEFs (EE NxN/7x7) well below the error-bars of the measurements. We remind that error-bars on the EEFs are calculated starting from Poissonian noise (see Sect. 2.2.1), and here the error-bars on the differences of the two images are taken as the sum of the error-bars of the two images, following propagation of errors.

In particular, we find on the whole FoV a mean ΔEEF1x1 = 0.43%, mean ΔEEF2x2 = 0.30%, mean ΔEEF5x5 = 0.03%. The dispersion of the values from the mean, calculated as the standard deviation (square root of the sum of squared differences from the mean divided by the size of the sample), has values of ΔEEF1x1 = 1.9%, ΔEEF2x2 = 0.6%, ΔEEF5x5 = 0.08%. We thus demonstrated that the PLATO EM performance is not suffering from stresses caused by thermal cycling issues.

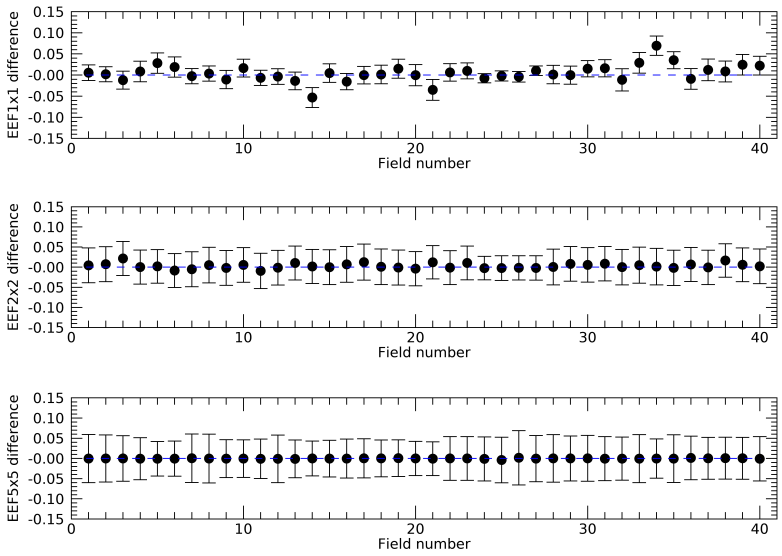

Figure 9: From top to bottom, differences for the EEF1x1, 2x2 and 5x5 pixels values taken before and after thermal cycling.

4. SUMMARY AND CONCLUSIONS

We tested the PLATO EM camera in a cryo-vacuum facility at SRON. In this manuscript we showed how we determined the best focus temperature of the PLATO EM camera, by using the two different methods of Hartmann mask and PSF analysis at different temperatures, which gave consistent results. The 5 temperatures plateaus we chose were found sufficient to derive the best focus temperature, which is of -77.6°C, perfectly matching the expectations and requirements.

We analysed the PSF on the whole FoV of the PLATO EM at the best focus temperature of -77.6°C. We performed analyses of the EEFs 1x1, 2x2 and 5x5 for all the 40 nominal positions that equally map the FoV, and we further verified the PSF behaviour at the edges of the FoV. We exclude from the verification of requirements the data taken on CCD3, which was affected by known configuration limitations, as the CAM EM CCDs are not flight like representative in term of performance. We also tested and verified the stability of the system after thermal cycling.

The Engineering Model camera was successfully integrated and validated under cryo-vacuum tests, allowing the mission to pass ESA's Critical Milestone, and confirming the mission is on track for launch in 2026.

ACKNOWLEDGMENTS

This work presents results from the European Space Agency (ESA) space mission PLATO. The PLATO payload, the PLATO Ground Segment, and PLATO data processing are joint developments of ESA and the PLATO Mission Consortium (PMC). Funding for the PMC is provided at national levels, in particular by countries participating in the PLATO Multilateral Agreement (Austria, Belgium, Czech Republic, Denmark, France, Germany, Italy, Netherlands, Portugal, Spain, Sweden, Switzerland, Norway, and United Kingdom) and institutions from Brazil. Members of the PLATO Consortium can be found at https://platomission.com/. The ESA PLATO mission website is https://www.cosmos.esa.int/plato. We thank the teams working for PLATO for all their work. INAF team acknowledges support from PLATO ASI-INAF agreement n. 2015-019-R.1-2018. The authors thank the Belgian Federal Science Policy Office (BELSPO) for the provision of financial support in the framework of the PRODEX Programme of the European Space Agency (ESA) under contract number PEA 4000137604.

REFERENCES

[1] Rauer, H., Catala, C., Aerts, C., Appourchaux, T., Benz, W., Brandeker, A., Christensen-Dalsgaard, J., Deleuil, M., Gizon, L., Goupil, M. J., Güdel, M., Janot-Pacheco, E., Mas-Hesse, M., Pagano, I., Piotto, G., Pollacco, D., Santos, Č., Smith, A., Suárez, J. C., Szabó, R., Udry, S., Adibekyan, V., Alibert, Y., Almenara, J. M., Amaro-Seoane, P., Eiff, M. A.-v., Asplund, M., Antonello, E., Barnes, S., Baudin, F., Belkacem, K., Bergemann, M., Bihain, G., Birch, A. C., Bonfils, X., Boisse, I., Bonomo, A. S., Borsa, F., Brandão, I. M., Brocato, E., Brun, S., Burleigh, M., Burston, R., Cabrera, J., Cassisi, S., Chaplin, W., Charpinet, S., Chiappini, C., Church, R. P., Csizmadia, S., Cunha, M., Damasso, M., Davies, M. B., Deeg, H. J., Díaz, R. F., Dreizler, S., Dreyer, C., Eggenberger, P., Ehrenreich, D., Eigmüller, P., Erikson, A., Farmer, R., Feltzing, S., de Oliveira Fialho, F., Figueira, P., Forveille, T., Fridlund, M., García, R. A., Giommi, P., Giuffrida, G., Godolt, M., Gomes da Silva, J., Granzer, T., Grenfell, J. L., Grotsch-Noels, A., Günther, E., Haswell, C. A., Hatzes, A. P., Hébrard, G., Hekker, S., Helled, R., Heng, K., Jenkins, J. M., Johansen, A., Khodachenko, M. L., Kislyakova, K. G., Kley, W., Kolb, U., Krivova, N., Kupka, F., Lammer, H., Lanza, A. F., Lebreton, Y., Magrin, D., Marcos-Arenal, P., Marrese, P. M., Marques, J. P., Martins, J., Mathis, S., Mathur, S., Messina, S., Miglio, A., Montalban, J., Montalto, M., Monteiro, M. J. P. F. G., Moradi, H., Moravveji, E., Mordasini, C., Morel, T., Mortier, A., Nascimbeni, V., Nelson, R. P., Nielsen, M. B., Noack, L., Norton, A. J., Ofir, A., Oshagh, M., Ouazzani, R. M., Pápics, P., Parro, V. C., Petit, P., Plez, B., Poretti, E., Quirrenbach, A., Ragazzoni, R., Raimondo, G., Rainer, M., Reese, D. R., Redmer, R., Reffert, S., Rojas-Ayala, B., Roxburgh, I. W., Salmon, S., Santerne, A., Schneider, J., Schou, J., Schuh, S., Schunker, H., Silva-Valio, A., Silvotti, R., Skillen, I., Snellen, I., Sohl, F., Sousa, S. G., Sozzetti, A., Stello, D., Strassmeier, K. G., Švanda, M., Szabó, G. M., Tkachenko, A., Valencia, D., Van Grootel, V., Vauclair, S. D., Ventura, P., Wagner, F. W., Walton, N. A., Weingrill, J., Werner, S. C., Wheatley, P. J., and Zwintz, K., "The PLATO 2.0 mission," *Experimental Astronomy* **38**, 249–330 (Nov. 2014).

[2] Ragazzoni, R., Magrin, D., Rauer, H., Pagano, I., Nascimbeni, V., Piotto, G., Piazza, D., Levacher, P., Schweitzer, M., Basso, S., Bandy, T., Benz, W., Bergomi, M., Biondi, F., Boerner, A., Borsa, F., Brandeker, A., Brändli, M., Bruno, G., Cabrera, J., Chinellato, S., De Roche, T., Dima, M., Erikson, A., Farinato, J., Munari, M., Ghigo, M., Greggio, D., Gullieuszik, M., Klebor, M., Marafatto, L., Mogulsky, V., Peter, G., Rieder, M., Sicilia, D., Spiga, D., Viotto, V., Wieser, M., Heras, A. M., Gondoin, P., Bodin, P., and Catala, C., "PLATO: a multiple telescope spacecraft for exo-planets hunting," in [*Space Telescopes and Instrumentation*

2016: Optical, Infrared, and Millimeter Wave], MacEwen, H. A., Fazio, G. G., Lystrup, M., Batalha, N., Siegler, N., and Tong, E. C., eds., *Society of Photo-Optical Instrumentation Engineers (SPIE) Conference Series* **9904**, 990428 (July 2016).

[3] Magrin, D., Ragazzoni, R., Rauer, H., Pagano, I., Nascimbeni, V., Piotto, G., Viotto, V., Piazza, D., Bandy, T., Basso, S., Benz, W., Bergomi, M., Biondi, F., Borsa, F., Börner, A., Brandeker, A., Brändli, M., Bruno, G., Cabrera, J., Calderone, F., Cessa, V., Chinellato, S., De Roche, T., Dima, M., Erikson, A., Farinato, J., Ghigo, M., Greggio, D., Klebor, M., Marafatto, L., Munari, M., Mogulsky, V., Pertenais, M., Peter, G., Portaluri, E., Rieder, M., Rockstein, S., Schweitzer, M., Sicilia, D., Umbriaco, G., Wieser, M., Heras, A. M., Marliani, F., Pirrotta, S., Salatti, M., Tommasi, E., Bardazzi, R., Battistelli, E., Brotini, M., Burresi, M., Capuano, E., Marinai, M., Novi, A., and Català, C., "PLATO: the ESA mission for exo-planets discovery," in [*Space Telescopes and Instrumentation 2018: Optical, Infrared, and Millimeter Wave*], Lystrup, M., MacEwen, H. A., Fazio, G. G., Batalha, N., Siegler, N., and Tong, E. C., eds., *Society of Photo-Optical Instrumentation Engineers (SPIE) Conference Series* **10698**, 106984X (July 2018).

[4] Pertenais, M., Cabrera, J., Paproth, C., Boerner, A., Grießbach, D., Mogulsky, V., and Rauer, H., "The unique field-of-view and focusing budgets of PLATO," in [*International Conference on Space Optics — ICSO 2020*], Cugny, B., Sodnik, Z., and Karafolas, N., eds., **11852**, 2043 – 2054, International Society for Optics and Photonics, SPIE (2021).

[5] Vandenbussche, B., Royer, P., Baeke, A., Regibo, S., Huygen, R., and et al., "The PLATO mission: camera thermal-vacuum performance verification and testing," in [*Society of Photo-Optical Instrumentation Engineers (SPIE) Conference Series*], *Society of Photo-Optical Instrumentation Engineers (SPIE) Conference Series* **12180**, 1218213 (Dec. 2022).

[6] Gorius, N. and et al., "Status of PLATO mission camera: recent progress on the camera engineering model and MAIV approach for the camera flight models," in [*Society of Photo-Optical Instrumentation Engineers (SPIE) Conference Series*], *Society of Photo-Optical Instrumentation Engineers (SPIE) Conference Series* **12180**, 1218046 (Dec. 2022).

[7] Pertenais, M., Cabrera, J., Griessbach, D., Erikson, A., Vandenbussche, B., Samadi, R., Reese, D., and Rauer, H., "Overview of PLATO's cameras on-ground and in-orbit calibration and characterisation," in [*International Conference on Space Optics — ICSO 2020*], Cugny, B., Sodnik, Z., and Karafolas, N., eds., **11852**, 97 – 109, International Society for Optics and Photonics, SPIE (2021).

[8] Cottinelli, A., Vassallo, D., Farinato, J., and Magrin, D. e., "Hartmann data analysis for PLATO TOU EM," in [*Society of Photo-Optical Instrumentation Engineers (SPIE) Conference Series*], *Society of Photo-Optical Instrumentation Engineers (SPIE) Conference Series* **12180**, 121802012 (Dec. 2022).